

## Vibrational electron spectroscopy of molecules in solids: Effect of the conduction-band density of states

M. Michaud, M. Lepage, and L. Sanche

*Département de Médecine Nucléaire et de Radiobiologie, Faculté de Médecine, Université de Sherbrooke, Québec, Canada, J1H 5N4*

(Received 21 January 1999)

The role of the conduction-band density of states (CB DOS) for electron scattering in the condensed phase is investigated using electron-energy-loss spectroscopy of a molecular target isolated in a host medium. As an experimental model we study  $O_2$  embedded in an Ar matrix, since  $O_2$  in the gas phase offers smooth resonant vibrational cross sections spanning most of the energy range where the CB DOS of solid Ar is known. The vibrational energy-loss intensities of matrix isolated  $O_2$  exhibit strong variations as a function of the incident energy (i.e., excitation functions), in contrast to its gas-phase counterpart. Except for a relative change in intensity, the features in the excitation functions remain essentially at the same energy for different scattering angles and follow the inverse of the CB DOS. We show that under resonant scattering condition this effect arises more specifically from changes in the resonance lifetime due to variations in the CB DOS of the host medium. Using a simple Boltzmann-type multiple-scattering analysis, the vibrationally scattered electron intensities from matrix-isolated species are further discussed in terms of transport phenomena subjected to the CB DOS. [S0163-1829(99)02324-3]

### I. INTRODUCTION

During the last three decades, electron resonant scattering or the formation of transient anion states has been considered to be the key mechanism responsible for strong vibrational excitations of molecules as well as dissociative electron attachment reactions induced by low-energy electrons in both gas<sup>1-3</sup> and condensed phase experiments.<sup>4-7</sup> An electron resonance occurs whenever an incident electron is captured into an empty orbital of an atom or a molecule during a time longer than the normal scattering time. Electron resonances are classified into two major categories: single particle or shape resonances, which consist of an incident electron trapped by a molecule in its ground state and two-particle one-hole or core-excited resonances, which consist of an incident electron trapped by a molecule in an excited state (e.g., the parent state). Electron trapping below or above the energy of the parent state is referred to as a Feshbach or a core-excited shape resonance, respectively.<sup>1</sup> Typical lifetimes of core-excited resonance are  $10^{-13}$  to  $10^{-15}$  s; those of shape resonances about  $10^{-14}$  to  $10^{-16}$  s. In the short-lifetime limit, we may have an efficient displacement of the nuclei prior to autodetachment and decay into a vibrationally excited ground or electronic state of the molecule. For longer lifetimes and repulsive anion states, we may have dissociation of the molecule into a negatively charged and one or more neutral fragments.

In gas-phase high-resolution electron-energy-loss (HREEL) spectroscopy, electron resonances are indicated by the selective excitation of vibrational modes, as well as strong variation in the incident energy dependence of the corresponding scattered electron intensities (i.e., excitation functions). Recent advances in the measurement of electron scattering cross sections in the gas phase<sup>8-12</sup> along with the availability of more elaborate theoretical calculations<sup>13-15</sup> proved to be profitable in understanding the vibrational and

electronic excitations of  $O_2$  by electron impact. Within the 0–3 eV range, the vibrational cross sections of  $O_2$  in the ground state are dominated by a series of sharp peaks due to the long lifetime and spin-orbit splitting of the  $^2\Pi_g$  resonance.<sup>9</sup> Above 5 eV, the cross sections are characterized by a broad band centered around 9 eV.<sup>9</sup> Several anion states related to the  $(\dots 1\pi_u^4 1\pi_g^2 3\sigma_u)$  electronic configuration have been calculated to lie within this energy range.<sup>16</sup> Among these, the short-lived  $^4\Sigma_u^-$  anion state, which as a quartet may only decay into the triplet ground state and thus not expected to be seen in the singlet states (e.g.,  $a^1\Delta_g, b^1\Sigma_g^+$ ), is the generally accepted candidate responsible for the vibrational enhancement. For the lowest electronic state  $a^1\Delta_g(v=0)$  both theoretical and experimental data indicate a gradual rise above threshold forming a broad band around 4 eV, which according to the theory<sup>15</sup> is due to the high-energy wing of the low-lying  $(\dots 1\pi_u^4 1\pi_g^3), ^2\Pi_g$  resonance. This feature is followed at about 8 eV by a broad peak with a high energy tail, which is predicted by theory to originate from the  $(\dots 1\pi_u^3 1\pi_g^4), ^2\Pi_u$  resonance. The latter resonance, being relatively long lived, is also responsible for the dissociative electron attachment process around 6.5 eV.<sup>8</sup>

Former HREEL measurements performed in this laboratory<sup>17</sup> showed that vibrational and electronic excitations of multilayer films of  $O_2$  condensed on a polycrystalline niobium substrate exhibited, as a function of the electron impact energy (i.e., excitation functions), broad resonances akin to those seen previously in the gas phase.<sup>18</sup> The lowest electronic state  $a^1\Delta_g(v=0)$ , which lies at an energy loss close to the  $v=4$  (i.e.,  $\sim 1$  eV), was found to have a resonance maximum around 7 eV followed by a high-energy tail. From the comparison with the gas-phase data, this resonance was then attributed primarily to the  $^2\Pi_u$  transient anion state whose potential energy curve is crossing the Franck-Condon region within the incident energy range 6–8 eV. The sharp features seen at low energy in the gas-phase vibrational cross

sections, and which are due to the  ${}^2\Pi_g$  resonance, were not observed in the condensed phase. While in the gas-phase vibrational cross sections, the resonance maximum above 5 eV did not vary with the exit vibrational channel, the energy at which the maximum vibrational enhancement occurred in the condensed phase appeared to shift from about 6 eV in the  $v=1$  up to 9.8 eV in the  $v=4$  channel of the  $X^3\Sigma_g^-$  state. This apparent shift of the resonance maximum with increasing  $v$  was attributed to a change in the admixture between the above  ${}^2\Pi_u$  transient anion state and the short-lived  ${}^4\Sigma_u^-$  anion state, whose potential curve is crossing the Franck-Condon region within the 8–12 eV range. Similarly to the gas phase, the latter resonance was not expected to decay into the electronic channel  $a^1\Delta_g$ .

In formal terms, an electron resonance is described as a discrete state embedded in a free-electron continuum.<sup>19</sup> By virtue of its coupling with that continuum, each discrete state of energy  $\varepsilon_d$  is shifted in energy by a small value  $\Delta$  and acquires an energy width  $\Gamma = \hbar/\tau$ , where  $\tau$  corresponds to the lifetime of the resonance.<sup>19,20</sup> More specifically, in the case of a diatomic molecule with  $R$  as the internuclear coordinate, a transient anion state is simply described in the fixed nuclei limit<sup>21,22</sup> by an energy- and  $R$ -dependent complex potential as

$$V_{\text{opt}}(R, E) = V_d(R) = \Delta(E) - \frac{1}{2}i\Gamma(E), \quad (1)$$

where  $V_d(R) \equiv \varepsilon_d(R) + V_G(R)$  is the potential energy curve of the discrete state,  $E = E_T - V_G(R)$  is the kinetic energy of the scattered electron with  $E_T$  the total energy of the system. The electronic decay width function  $\Gamma(E)$  is given explicitly by

$$\Gamma(E) = \hbar/\tau(E) = 2\pi \sum_{\mathbf{k}} |V_{d,\mathbf{k}}|^2 \delta(E - E_{\mathbf{k}}) \cong 2\pi |V_{d,E}|^2 D(E), \quad (2)$$

where  $V_{d,\mathbf{k}}$  is the coupling matrix element responsible for the decay and  $E_{\mathbf{k}}$  the energy of the free-electron continuum. Under sufficiently small variations of the matrix element with the wave vector  $\mathbf{k}$ , the density of free-electron states  $D(E)$  appears explicitly with the summation over  $\mathbf{k}$ .<sup>23</sup>

The origin of the vibrational excitation can be rationalized with the following semiclassical considerations. Defining the resonant transition energy according to  $E_r(R) \equiv ReV_{\text{opt}}[R, E_r(R)] - V_G(R)$ , one may further reduce  $V_{\text{opt}}(R, E)$  to an  $R$ -only dependent complex potential

$$V_{\text{opt}}(R) = V_d(R) + \Delta[E_r(R)] - \frac{1}{2}i\Gamma[E_r(R)]. \quad (3)$$

Since  $V_{\text{opt}}(R) - V_G(R)$  is usually not constant, the energy of a resonance can be seen to be, in effect, tunable with a small change of the internuclear distance  $R$ . The available energy range is essentially limited by the overlap of the nuclear wave function of the transient anion with that of the ground state (i.e., the Franck-Condon factor). Alternatively, this energy range can be seen as the result of resonant scattering events taking random snapshots of a molecule whose resonance energy fluctuates due to the nuclear motion about the equilibrium position in the ground state. In the case of the  ${}^4\Sigma_u^-$  anion state of  $\text{O}_2$ , the energy range can be as large as 10 eV.

As such, the amplitude of the vibrational excitation or the probability of overtone excitations, is connected to the energy imparted to the nuclei  $\Delta T_N$ . In the short capture-time limit,  $\Delta T_N$  can be calculated from the classical work done while the molecule evolves along the shifted anion potential energy curve  $V_r(R) = V_d(R) + \Delta[E_r(R)]$  from an initial ( $R_i$ ) to a final ( $R_f$ ) nuclear coordinate. Assuming for simplicity, a zero initial nuclear velocity from the ground electronic state, a small nuclear displacement in the anion state with a constant force  $F_r(R_f) \cong F_r(R_i) = dV_r(R)/dR|_i$  and a fixed lifetime  $\tau[E_r(R_i)] \cong \tau[E_r(R_f)]$ , we readily obtain

$$\Delta T_N \cong (2M_{\text{red}})^{-1} F_r^2(R_i) \tau^2[E_r(R_i)], \quad (4)$$

where  $M_{\text{red}}$  is the reduced mass of the molecule corresponding to the nuclear coordinate  $R$ . The energy imparted to the nuclei  $\Delta T_N$  is thus a combination of two factors: the strength of the resonant vibrational coupling  $F_r(R)$  and the resonance lifetime  $\tau[E_r(R)]$ . The former factor, which is derived from the potential energy curve  $V_d(R)$ , describes the response of the nuclei when the electron is mostly localized on the molecule. The latter factor, which is connected to the density of states  $D(E)$  [cf. Eq. (2)], is particularly sensitive to the behavior of the electron outside the target and hence, to the host medium.

In the gas phase (i.e., vacuum), the energy dependence of  $D(E)$  has a monotonous behavior. The same is not true in the condensed phase especially when the electron wavelength is of the same order of magnitude as distance between the scatterers. More specifically in an ordered solid, a propagating electron, which experiences multiple elastic scatterings, becomes a Bloch electron whose energy  $E_{\mathbf{k}}$  as a function of its wave vector  $\mathbf{k}$  defines an energy-band structure.<sup>24</sup> The conduction-band density of states (CB DOS) is defined whenever a quantity that depends on the electron wave vector through  $E_{\mathbf{k}}$  is averaged over all directions of  $\mathbf{k}$ .<sup>24</sup> The energy dependence of the CB DOS differs substantially from solid to solid and usually presents pronounced variations compared to the monotonous behavior of its gas-phase counterpart. The CB DOS is best understood theoretically<sup>25</sup> and experimentally<sup>26,27</sup> in large band-gap materials such as rare gas solid (RGS). In the case of pure solid films of Ar, Kr, and Xe,<sup>28,29</sup> we found that the energy dependence of the energy-loss intensity arising from multiple scattering on phonons and defects can virtually reproduce the CB DOS up to about 14 eV above the vacuum level, as calculated by Bacalis, Papaconstantopoulos, and Pickett.<sup>30</sup>

In this paper, we extend our recent work<sup>31</sup> where the effect of the CB DOS on the electron resonance lifetime and its impact on the energy deposited in a molecule was reported. We proposed to monitor the deposited energy by looking at the electron-induced vibrational excitations of a molecular target isolated in a host medium that offers a free-electron continuum different from the vacuum. As an experimental model, we chose to embed  $\text{O}_2$  in an ordered solid Ar matrix, since  $\text{O}_2$  in the gas phase offers smooth vibrational cross sections arising from the relatively short-lived  ${}^4\Sigma_u^-$  anion state, which covers most of energy range where the CB DOS of solid Ar is known. In the present work, we first investigate the incident energy dependence of the vibrational and electronic excitations of a multilayer solid film of  $\text{O}_2$  condensed

on the Pt(111) substrate. This is followed by a study of the crystal structure of the pure and O<sub>2</sub>-doped solid films of Ar deposited under the same conditions. Then, the vibrational HREEL spectroscopy of matrix isolated O<sub>2</sub> is presented as a function of the incident energy for different scattering angles and matrix-film thicknesses. Using a simple Boltzmann-type multiple-scattering analysis, the experimental results are discussed in connection to changes in the electron scattering cross section and electron-transport property. The vibrational excitation function are separated into two phenomenological contributions: (a) an extrinsic contribution identified merely as an energy-dependent superimposed phonon background, which follows the variation in the CB DOS of the host medium, and (b) an intrinsic contribution that manifests as a modulation of the scattered intensities with incident energy, which correlates to the *inverse* of the CB DOS. The origin of the latter contribution is further shown to be essentially two-fold. First, under electron resonant scattering conditions, changes in the electron scattering cross section is observed as distinct intensity changes among the energy losses, such as selective vibrational excitations. This is shown to result more specifically from changes in the resonance lifetime (i.e., lifetime of an isolated anion specie) due to variations in the CB DOS of the host medium. Second, at sufficient high-film thickness, the electron transport property is found to be responsible for a common and limited modulation of the vibrational scattered intensities that may follow the inverse of the CB DOS.

## II. EXPERIMENT

### A. Apparatus

The electron-scattering measurements were performed with an improved HREEL spectrometer of the type previously described<sup>32</sup> and that consists of two hemispherical electrostatic energy selectors (i.e., monochromator and analyzer). The angle of incidence  $\theta_0$  of the monochromator can be varied between 8° and 90° from the normal to the sample. The angle of analysis  $\theta_d$  of the analyzer is fixed at 45° at the opposite azimuth. Double-zoom electron lenses at the exit of the monochromator and at the entrance of the analyzer were adjusted so as to allow the recording of an excitation function over the widest possible incident energy range (e.g., 1–19 eV) allowing minimal variation in the transmission of the instrument. In the present experiment, the combined resolution of the selectors was set at 15 meV full width at half maximum (FWHM) for a current of 0.3 nA on the sample. The incident electron energy  $E_0$  was calibrated within  $\pm 0.1$  eV with respect to the vacuum level by measuring the threshold of the electron current transmitted through the samples. Sample charging or decomposition could be detected from comparing the spectra recorded at different time intervals.

The apparatus is also equipped with a reflection high-energy electron diffraction (RHEED) gun (Kimball Physics), which aims the sample at a glancing incidence, and a resistive-anode imaging detector (Surface Sciences). The latter can be positioned to collect either the RHEED image or the low-energy electron diffraction (LEED) pattern for an energy just above the emergence of the diffracted beams in vacuum. The whole system is housed into an UHV chamber

maintained at a base pressure of  $8 \times 10^{-11}$  Torr by the combined action of an ion pump and a liquid-N<sub>2</sub> cooled titanium sublimation pump.

### B. Samples preparation

The samples initially prepared in a gas-handling manifold are condensed from the gas or vapor phase onto a Pt(111) single crystal (Johnson and Matthey) attached on a low-temperature sample manipulator. The latter, which has been described in details previously,<sup>33</sup> allows cooling to 16 K and heating up to 1100 K, as well as  $\pm 100^\circ$  azimuthal rotation, 50° flip, and  $\pm 0.5$ -cm X, Y, and Z translations of the sample. The gas-handling manifold consists of two different sources connected to a small calibrated volume through bypass and precision-leak valves. This volume is connected via an admission valve to a capillary having an opening located close to the crystal. The crystal was cleaned by sequences of sputtering with Ar<sup>+</sup> ions followed by annealing and heating in the presence of oxygen at about 900 K. These treatments gave HREEL spectra free from vibrational energy losses due to contaminating atoms or molecules. The crystal could be further characterized from the observation of LEED threshold interference structures present in the energy dependence of the specular beam intensity (i.e., 00 beam at  $\theta_0 = \theta_d = 45^\circ$ ).<sup>34</sup> Its orientation was determined from the energy dispersion of the threshold interference structures as a function of the incident azimuthal angle  $\phi_0$  along with the intensity of the emerging diffracted beams.<sup>35</sup> Because of the symmetry seen in the present experiment, the azimuthal angle was limited to the range  $0^\circ \leq \phi_0 \leq 60^\circ$ , where emergence of the ( $\bar{1}0$ ) and ( $0\bar{1}$ ) beams occurs.

The O<sub>2</sub> and Ar gases were supplied by Matheson of Canada Ltd. with a stated purity of 99.998% and 99.9995%, respectively. The purity of the leaked gases was monitored by a quadrupole mass spectrometer (0–200 amu) facing the crystal. The thickness of the deposited film or the number of condensed layers was estimated at  $\pm 10\%$  from the calibrated amount of gas needed to deposit a monolayer, assuming no change of the sticking coefficient for the adlayers, as previously described.<sup>36,37</sup> Furthermore, from the observation of the elastic specular intensity as a function of the azimuthal angle, the Ar film was found to grow on Pt(111) in an ordered hcp arrangement with minimal addition of defects up to 50 layers.

A well-known method to study isolated molecules in the condensed phase consists of trapping a small amount of the species of interest into RGS matrix at very low temperature. This technique has been developed over the past three decades particularly for the investigation of unstable and very reactive systems.<sup>38</sup> Owing to our method of sample preparation, we choose to isolate O<sub>2</sub> in solid films of Ar, which offers a comparable atomic mass and condensation temperature. In practice,  $10^{-3}$  Torr of O<sub>2</sub> and  $10^{-1}$  Torr of Ar were mixed together in the calibrated volume from which a small amount ( $1-20 \times 10^{-3}$  Torr) was condensed onto the crystal held at a temperature of 16 K. The accuracy of the present mixture may vary from an experiment to another by about  $\pm 20\%$ .

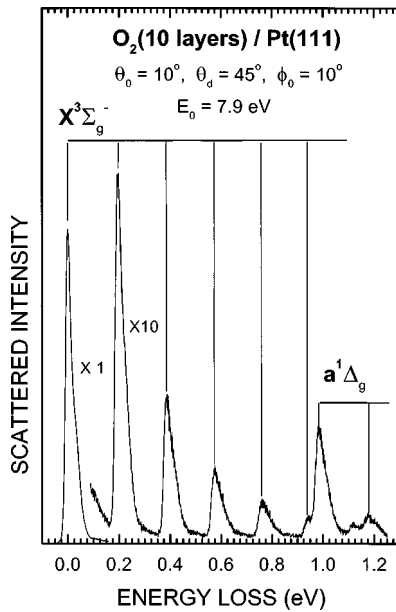


FIG. 1. High-resolution electron-energy-loss spectrum of a 10-layer film of  $O_2$  condensed on Pt(111) for an incident electron energy of 7.9 eV. The angle of incidence  $\theta_0$  was set at  $10^\circ$  with the azimuth  $\phi_0$  at  $10^\circ$  and the analyzer  $\theta_d$  fixed at  $45^\circ$ .

### III. RESULTS

#### A. Pure solid film of $O_2$

With the present instrument, we reinvestigated electron-induced vibrational and electronic excitation of  $O_2$ , for the case of multilayer films of  $O_2$  condensed on the Pt(111) surface. We show in Fig. 1 the HREEL spectrum for a 10-layer film and an incident electron energy of 7.9 eV. The angle of incidence  $\theta_0$  was set at  $10^\circ$ , the azimuth  $\phi_0$  at  $10^\circ$ , and the analyzer fixed at  $45^\circ$ . The large peak near zero-energy loss corresponds to the electron scattered elastically and quasielastically (i.e., phonon scattering) from the film. The smaller peaks with a separation of about 0.2 eV are ascribed to the vibrational progression ( $v=1,2,3, \dots$ ) of the molecule in its ground state  $X^3\Sigma_g^-$ . The peak at 0.98 and 1.18 eV are excitations of the  $v=0$  and 1 in the lowest electronic state  $a^1\Delta_g$ . The incident electron-energy dependence of the major losses is shown in Fig. 2 for the same film thickness and scattering angles. Also shown in this figure is the scattered electron intensity of the inelastic background located just before the  $v=1$  peak onset at  $\Delta E=0.16$  eV along with that contributing to each energy loss (dashed lines). Although performed on a single-crystal substrate and for a different scattering geometry, the present excitation functions are comparable to our former measurements<sup>17</sup> with the maxima having generally the same relative intensities and energies.

The excitation function for the  $a^1\Delta_g(v=0)$  loss in Fig. 2 bears some resemblance to the gas-phase experimental and theoretical data. The closest similitude is found with the energy dependence of the differential cross section measured at  $90^\circ$  scattering angle.<sup>8</sup> In the present measurement, however, the  $^2\Pi_u$  resonance maximum is found at a slightly lower energy (i.e., 6.8 eV) and the 4-eV feature akin to the wing of the  $^2\Pi_g$  resonance is more shallow. The shift of the resonance can be mostly accounted for by the electronic polar-

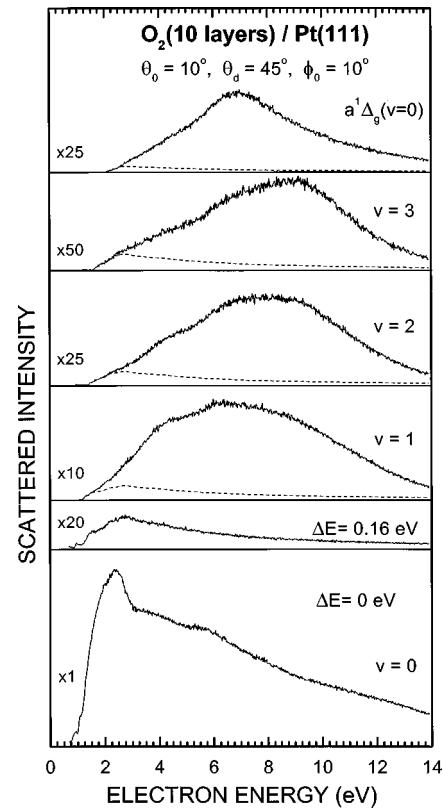


FIG. 2. Electron impact energy dependence of the  $X^3\Sigma_g^-$ ,  $v=0,1,2,3$  vibrational, and the  $a^1\Delta_g(v=0)$  electronic loss scattered intensities from a 10-layer film of  $O_2$  condensed on Pt(111). The angle of incidence  $\theta_0$  was set at  $10^\circ$  with the azimuth  $\phi_0$  at  $10^\circ$  and the analyzer  $\theta_d$  fixed at  $45^\circ$ . Also shown is the energy dependence of the inelastic background intensity located just before the  $v=1$  loss peak onset at  $\Delta E=0.16$  eV along with that contributing to each energy-loss profile (dashed lines).

ization of the surrounding medium by the anion (i.e., electronic polarization energy). A polarization energy value of 1–2 eV is typical of van der Waal solids. On the other hand, the small appearance of the 4-eV feature may be due to the comparison between the gas and the solid not being made at exactly the same scattering angle. In fact, the angular dependence of the  $a^1\Delta_g(v=0)$  gas-phase cross section, which exhibits maxima around  $0^\circ$  and  $180^\circ$  along with a small hump near  $90^\circ$ , actually goes through a minimum at  $125^\circ$ , which corresponds to the present scattering angle.

The vibrational excitation functions of  $O_2$  in the solid phase differ in many respects from the gas-phase results. First, the well-known sharp peaks due to the  $^2\Pi_g$  resonance, which dominate the vibrational cross sections up to 3 eV in the gas phase,<sup>9</sup> are notoriously absent in the solid phase. Furthermore, as one can see in Fig. 2, the excitation functions for the  $X^3\Sigma_g^-$ ,  $v=1,2,3$  vibrational losses are characterized by three broad overlapping bands compared to one in the gas phase. The second band has its maximum at about 6.5 eV in the  $v=1$  channel, whereas the third one is found around 9.3 eV in the  $v=3$ . The magnitude of the former band, decreases more rapidly than the latter with increasing vibrational number, thus producing an apparent shift of the overall resonance maximum. In analogy with the gas-phase assignment, the 9.3-eV feature, which is also absent in the

$a^1\Delta_g(v=0)$  excitation function, is ascribed to the  $^4\Sigma_u^-$  transient anion state. The 6.5 eV feature, which corresponds to the energy of the maximum in the  $a^1\Delta_g(v=0)$  excitation function, is attributed to the  $^2\Pi_u$  resonance as in our former study. This assignment is actually substantiated with the recent gas-phase<sup>9</sup> data where the presence of a weak shoulder at about 8 eV in the vibrational cross sections for higher overtone modes ( $v=6-8$ ) agrees with the  $^2\Pi_u$  resonance maximum in the  $a^1\Delta_g(v=0)$  channel. Finally, there is in the vibrational profile of Fig. 2, what seems to have been overlooked in our former results,<sup>17</sup> a shoulderlike feature (i.e., first band) around 4 eV. The latter appears to be of the same origin as the 4-eV feature observed in the  $a^1\Delta_g(v=0)$  profile in both gas- and solid-phase data. At first glance a vibrational enhancement within the 2–5 eV incident energy range is rather surprising since in the gas phase,<sup>9</sup> except for a very small and continuous signal in the  $v=1$  cross section, there is virtually no intensity in the overtone channels throughout this incident energy range. The presence of this new feature along with the absence of the sharp peaks at low energy in the solid phase may well be due to the lowering of the  $^2\Pi_g$  anion state by the electronic polarization of the surrounding medium. For instance, if the  $^2\Pi_g$  anion potential energy curve is shifted down with a new location at about 1 eV below the  $X^3\Sigma_g^-$  neutral ground state at the equilibrium position in the solid phase; then the resulting energy separation as a function of the internuclear distance is similar to that between the same anion state and the  $a^1\Delta_g$  electronic state in the gas phase. Hence, in analogy to the excitation mechanism for the  $a^1\Delta_g$  electronic state in the gas phase, only the high-energy wing of the  $^2\Pi_g$  resonance with no sharp structure would contribute to the vibrational excitation in the solid phase.

It should be noticed, however, that a contribution from the  $\Sigma^+$  transient anion states, which are forbidden by the mirror plane symmetry selection rule in the gas phase (i.e.,  $\Sigma^- \leftrightarrow \Sigma^+$ ), cannot be excluded here owing to the loss of the cylindrical symmetry of  $O_2$  in the condensed phase. Evidence of the relaxation of this rule was originally given by Azria, Parenteau, and Sanche<sup>39</sup> from ion kinetic energy and electron-energy-dependence measurements of the  $O^-$  yield from condensed  $O_2$ . In contrast to the measurements in the gas phase, where a single peak assigned to the  $^2\Pi_u$  resonance is found around 6.5 eV, the condensed phase  $O^-$  yield is showing several features at about 6.5, 8.5, 10.5, and 13.5 eV and generally ascribed to  $^2\Pi_u$ ,  $^2\Sigma_g^+(I)$ ,  $^2\Sigma_u^+(I)$ , and  $^2\Sigma_{g,u}^+(II)$  anion states, respectively.

### B. Pure solid film of Ar

We searched for the crystal structure of 10 to 50-layer solid film of Ar deposited on the Pt(111) by monitoring the LEED patterns for several incident angles and energies. The diffracted spots displayed the hexagonal geometry (i.e., threefold crystal axis) expected for a film growth along the normal to the (111) planes of a fcc single crystal of Ar. The diffracted beams were found at exactly the same azimuth but emerged for an incident energy lower than their Pt(111) counterparts. In Fig. 3, we show the energy dependence (2–14 eV) of the specular elastic reflection (i.e., 00 beam at

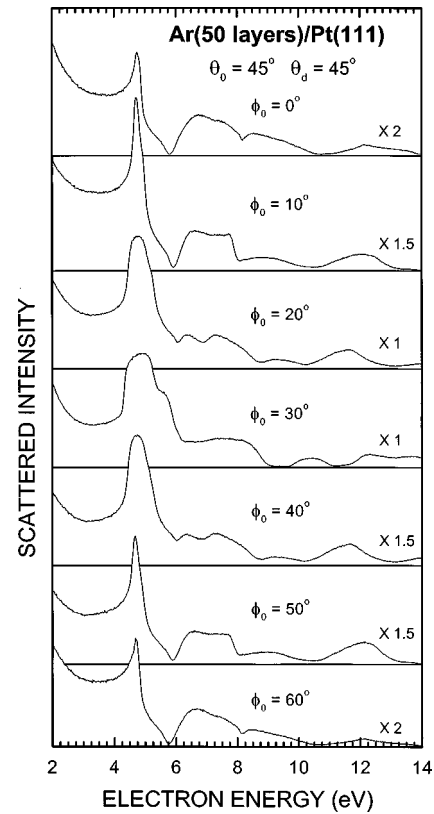


FIG. 3. Energy dependence of the specular reflection of the incident electron beam (i.e., 00 beam at  $\theta_0 = \theta_d = 45^\circ$ ) from a 50-layer film of Ar condensed on Pt(111) as a function of the azimuthal orientation of the crystal  $\phi_0$ . We note that the profile is the same already after a  $\phi_0 = 60^\circ$  rotation (i.e., sixfold rotation axis) and shows a mirror symmetry about  $\phi_0 = 30^\circ$ .

$\theta_0 = \theta_d = 45^\circ$ ) from a 50-layer Ar film as a function of the azimuthal angle  $\phi_0$ . We note that the profile is the same after only a  $\phi_0 = 60^\circ$  rotation (i.e., sixfold rotation axis) and shows a mirror symmetry about  $\phi_0 = 30^\circ$ . As first pointed out by Woodruff and Holland,<sup>40</sup> one may recognize here the outcome of the time-reversal invariance or the reciprocity theorem.

The reciprocity theorem, which applies in many areas of physics, leads to symmetries over and above those arising from the mere crystal structure. More specifically in the case of a fcc (111) single crystal, the combination of time-reversal symmetry and the threefold axis gives rise to a sixfold symmetry axis for the 00 beam. The same is true as well in the computation of the specular elastic reflection of the semi-infinite Ar(111) crystal, as we previously verified in Ref. 37. Calculations of the 00 beam intensity, which are plotted in Fig. 4(b) of that work, were performed for the same scattering angles and incident energy range as in the present experiment. Above 12 eV no correction for the additional absorption due to energy losses to electronic excitations were included. Except for the absence of the sharp peak at 4.7-eV, which develops only around  $\phi_0 = 0^\circ$  and  $60^\circ$ , there is a good correlation between the calculated and present experimental profiles. Moreover, the overall large specular reflectivity below 6 eV with the broad maximum around 5 eV are reasonably reproduced.

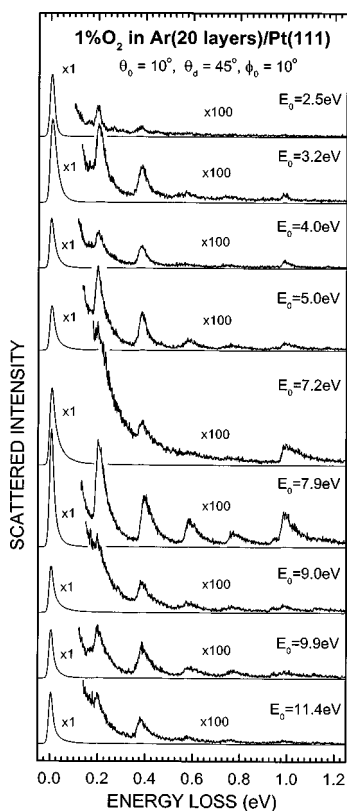


FIG. 4. Vibrational electron-energy-loss spectra of a 20-layer film of 1%  $O_2$  in Ar deposited on Pt(111) for different incident energies  $E_0$ . The angle of incidence  $\theta_0$  was set at  $10^\circ$  with the azimuth  $\phi_0$  at  $10^\circ$  and the analyzer  $\theta_d$  fixed at  $45^\circ$ . The scattered intensity scale, although arbitrary in absolute intensity, and the magnification factors are the same for all recordings.

### C. Molecules of $O_2$ isolated in an Ar matrix

We investigated solid Ar doped with up to 1.5% of  $O_2$  under identical conditions of temperature, deposition rate, and film thicknesses (i.e., 10 to 50 layers) as in the previous section. The same LEED pattern and specular reflectivity profiles were observed therefore indicating that, for a sufficiently low-impurity concentration, the crystal structure of the matrix film corresponds to that of the pure solid film.

#### 1. High-resolution electron-energy-loss spectra

In Fig. 4, we report the HREEL spectra of a 20-layer film of 1%  $O_2$  in Ar for different incident energies. The angle of incidence  $\theta_0$  was set at  $10^\circ$  and the azimuth  $\phi_0$  at  $10^\circ$  with the analyzer fixed at  $45^\circ$ . The scattered intensity scale, although arbitrary in absolute intensity, and the magnification factors are the same for all recordings. In all spectra, the large peak near zero energy loss ( $\Delta E = 0$  eV) corresponds to the electrons scattered elastically and quasielastically from the film. The exact peak position and the extent of the energy-loss tail on the right side, which arises essentially from multiple losses to phonon modes of the matrix (i.e., the phonon background), both depend on the incident energy. With an intensity gain of 100, the vibrational progression ( $v = 1, 2, \dots$ ) of  $O_2$  in its ground state  $X^3\Sigma_g^-$  and the lowest electronic transition  $a^1\Delta_g$  at 0.98 eV are easily revealed. The weak additional structures appearing in the 0.2–0.4 eV

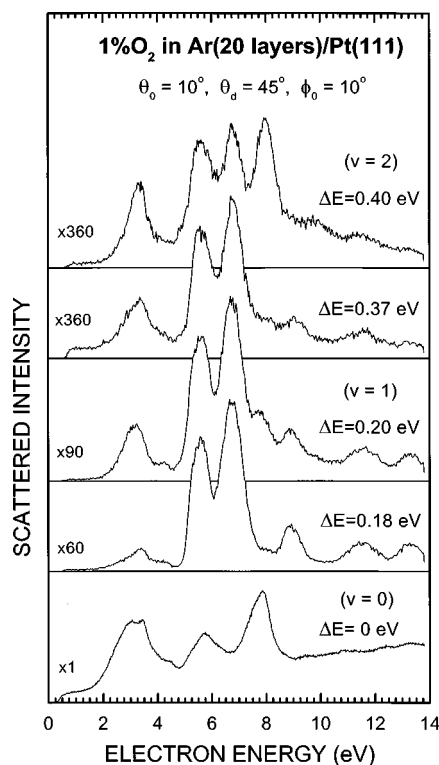


FIG. 5. Electron impact energy dependence of the quasielastic peak ( $\Delta E = 0$  eV) and the  $v = 1, 2$  vibrational losses for a 20-layer film of 1%  $O_2$  in Ar deposited on Pt(111). The angle of incidence  $\theta_0$  was set at  $10^\circ$  with the azimuth  $\phi_0$  at  $10^\circ$  and the analyzer  $\theta_d$  fixed at  $45^\circ$ . Also shown is the energy dependence of the phonon background intensity (i.e., multiple losses to phonons) at  $\Delta E = 0.18$  and  $0.37$  eV, and which are located just before the  $v = 1, 2$  peak onsets.

energy-loss range of the  $E_0 = 2.5$  eV spectrum are merely due to traces of  $N_2$  and CO, which both possess extremely large vibrational cross sections within 1–3 eV incident energy. The intensity of the  $O_2$  vibrational and electronic losses, which are superimposed on the phonon background, is strongly dependent on small differences in the incident energy as one can immediately see from comparing the spectra at  $E_0 = 7.9$  eV with that at  $E_0 = 7.2$  or 9 eV.

#### 2. Excitation functions for different electron-energy losses

To better illustrate the variations in the vibrational excitations for different  $E_0$ , we recorded the scattered electron intensity as a function of the incident energy for a few selected energy losses. We display in Fig. 5, for the same matrix and scattering angles as in Fig. 4, the excitation function for the elastic peak ( $\Delta E = 0$  eV) and the  $v = 1, 2$  vibrational losses. Also shown in this figure is the energy dependence of the phonon background intensity (i.e., multiple losses to phonons) at  $\Delta E = 0.18$  and  $0.37$  eV, which are located just before the  $v = 1, 2$  peak onsets, respectively.

The excitation function for the elastic peak reveals several maxima, which either disappear or change position with the angle of incidence  $\theta_0$ . This can be seen by comparing the elastic profile measured at  $\theta_0 = 10^\circ$  in Fig. 5 with the result at  $\theta_0 = 60^\circ$  and for  $\phi_0 = 10^\circ$  in Fig. 6. This is also true upon changing the azimuthal angles as one can further see from

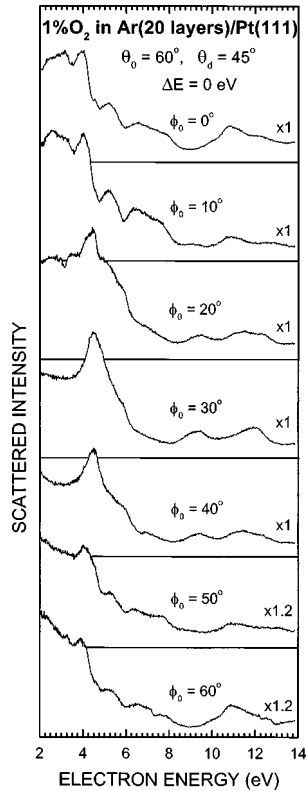


FIG. 6. Electron impact energy dependence of the quasielastic scattered intensity ( $\Delta E=0$  eV) from a 20-layer film of 1%  $O_2$  in Ar deposited on Pt(111) for an angle of incidence  $\theta_0=60^\circ$  and analysis  $\theta_d=45^\circ$  as a function of the azimuthal orientation of the crystal  $\phi_0$ .

the  $\phi_0=0^\circ$  and  $\phi_0=30^\circ$  recordings in Fig. 6. This behavior is attributed to coherent multiple elastic scattering process that is also responsible for the LEED features in a well-ordered solid film. Still, the profiles in Fig. 6 bear a resemblance after a  $\phi_0=60^\circ$  rotation (i.e., sixfold rotation axis) and show a mirror symmetry about  $\phi_0=30^\circ$ .

In contrast to the  $O_2$  results in the gas phase<sup>9</sup> as well as in the pure solid film (Fig. 2), the excitation functions for the  $v=1$  and 2 vibrational losses in Fig. 5 are much more structured with the presence of many narrow features. From comparing to their respective phonon background excitation functions at  $\Delta E=0.18$  and 0.37 eV, one can ascribe at once the origin of some of these features to the phonon background emerging in the vibrational excitation functions. This phenomenon is due to the relatively large intensity of the phonon energy-loss tail, which extends from the elastic peak to the  $v=1$  loss and beyond. For instance, we estimate from Fig. 4 that this energy-loss tail contributes to about 30% (10%) of the  $v=1$  (2) intensity at the incident energy of 7.9 eV, and up to  $\sim 90\%$  ( $\sim 60\%$ ) at both 7.2 and 9.0 eV incident energies. It should be noted that this effect is not limited only to the matrix-film experiment and that the same phenomenon can arise in pure molecular film as we found previously in the vibrational HREEL spectroscopy of solid  $N_2$ .<sup>41</sup> Owing to the relatively small  $O_2$  concentration, the present features in the phonon background excitation functions are almost the same as those observed in pure solid films of Ar.<sup>28,29</sup> In the latter case, we showed<sup>28,29</sup> that such energy-dependent features actually reflects the theoretical<sup>30</sup> CB DOS above the

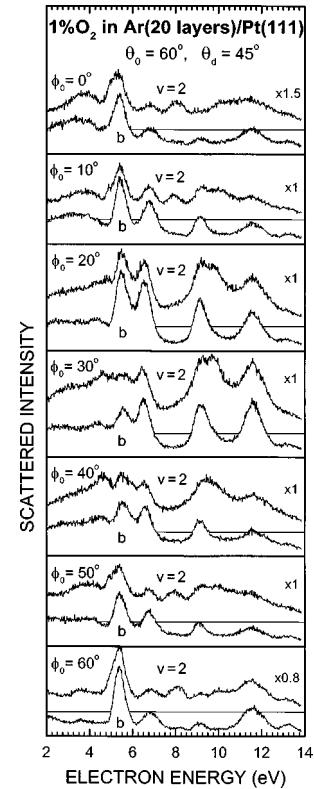


FIG. 7. Electron impact energy dependence of the  $v=2$  vibrational scattered intensity and phonon excitation function (labeled *b*) from a 20-layer film of 1%  $O_2$  in Ar deposited on Pt(111) for an angle of incidence  $\theta_0=60^\circ$  and analysis  $\theta_d=45^\circ$  as a function of the azimuthal orientation of the crystal  $\phi_0$ .

vacuum level. Experimentally, a key characteristic of these CB DOS features is that they grow slowly with the thickness of the RGS film.<sup>29</sup>

The vibrational excitation functions in Fig. 5 reveal, besides the features related to the phonon background, several new features: two relatively intense ones at 3.2 and 7.9 eV, a smaller one at 9.9 eV, and a shoulder at 5 eV. These new features may be classified as *belonging solely* to a  $O_2$  vibrational excitation function (i.e., *intrinsic*) as opposed to those akin to the phonon background (i.e., *extrinsic*), which being merely *additive* is not truly part of the vibrational scattered intensity. Except for a relative change in intensity, however, both the intrinsic and extrinsic features remain at the same energy upon increasing  $\theta_0$ . This can be seen from comparing the vibrational and phonon excitation functions (labeled *b*) pertaining to the  $v=2$  mode at  $\theta_0=10^\circ$  and  $\phi_0=10^\circ$  in Fig. 5 to the same ones but recorded for  $\theta_0=60^\circ$  in Fig. 7. In the latter figure the azimuthal angle values are exactly the same as for the elastic peak in Fig. 6. It should be further mentioned that to avoid spurious charging effects, a different azimuthal recording was performed on a new matrix preparation, which may admit slight variations in both  $O_2$  concentration and film thickness. Bearing in mind these experimental limitations, one can see for both the  $v=2$  and the phonon excitation functions about the same characteristic profiles after a  $\phi_0=60^\circ$  rotation and nearly a mirror symmetry about  $\phi_0=30^\circ$ . At first glance this observation may be rather surprising since, unlike elastic scattering, multiple inelastic scattering within an ordered film is an incoherent process and as

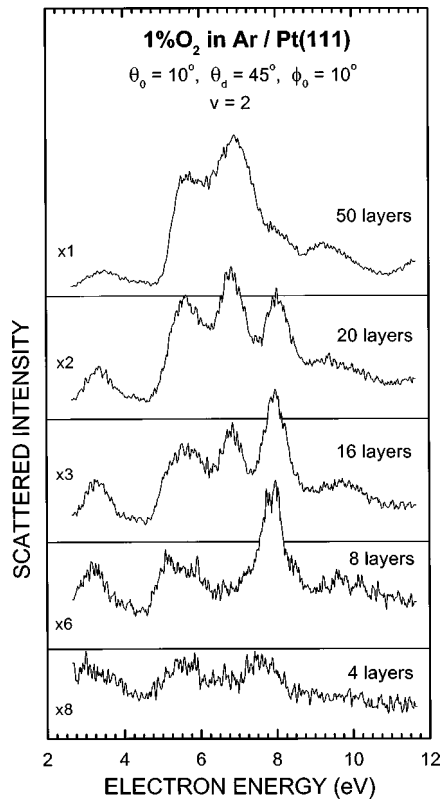


FIG. 8. Electron impact energy dependence of the  $\nu=2$  vibrational scattered intensity from 1%  $\text{O}_2$  in Ar deposited on Pt(111) as a function of the film thickness. The angle of incidence  $\theta_0$  was set at  $10^\circ$  with the azimuth  $\phi_0$  at  $10^\circ$  and the analyzer  $\theta_d$  fixed at  $45^\circ$ .

such is not expected to be sensitive to crystal orientation. However, as discussed in further details in the next section, an incoherent process is actually subjected to an entrance ( $P_{\text{en}}$ ) and then to an exit ( $P_{\text{ex}}$ ) probability at the solid-vacuum interface for a given scattering geometry. These probabilities arise essentially from the specular elastic reflection (i.e., 00 beam) along with the presence of diffracted beam intensities. Although in general  $P_{\text{en}}$  and  $P_{\text{ex}}$  vary differently with the electron energy, their azimuthal dependence is reflecting the same symmetry properties at the surface of the crystal.

More importantly, the intrinsic features in a vibrational excitation function differ experimentally from the extrinsic ones as they grow and saturate more quickly with the thickness of the film. In Fig. 8, the  $\nu=2$  excitation function is reported as a function of the film thickness for the same geometrical scattering conditions as in Fig. 5. As one can immediately see, the intrinsic features are already visible within the 4–8-layer range whereas the extrinsic ones emerge only for larger film thicknesses. At 20 layers, the intrinsic features are superimposed on the phonon background, which under the present energy loss, reflects the CB DOS. The features in the phonon background grow steadily with the film thickness, up to about 50 layers, where they largely dominate the excitation function with an overall intensity about twice as large as that at 20 layers.

The incident electron-energy dependence of the net intensity of the  $\nu=1$  and 2 vibrational loss, resulting from the subtraction of the corresponding phonon background (Fig. 5), is shown in Fig. 9(a). The short vertical bars indicate the

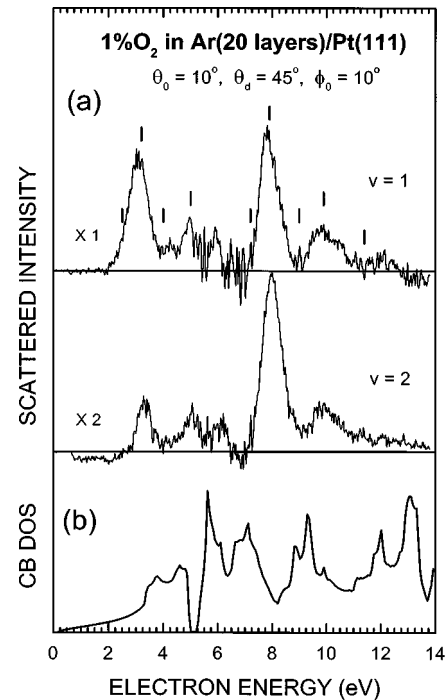


FIG. 9. (a) Electron impact energy dependence of the net  $\nu=1$  and 2 vibrational intensities, resulting from the subtraction of the corresponding phonon background, for a 20-layer film of 1%  $\text{O}_2$  in Ar deposited on Pt(111). The angle of incidence  $\theta_0$  was set at  $10^\circ$  with the azimuth  $\phi_0$  at  $10^\circ$  and the analyzer  $\theta_d$  fixed at  $45^\circ$ . The short vertical bars indicate the incident energies at which the energy-loss spectra of Fig. 4 were recorded. (b) Conduction-band density of states (CB DOS) for the fcc structure of solid Ar as calculated in Ref. 30.

incident energies at which the HREEL spectra of Fig. 4 were recorded. For  $\nu=2$ , the resulting curve correlates well to the excitation function at 8 layers in Fig. 8, where mostly the intrinsic features can be observed since the CB DOS features are still not fully developed. Except for a relative intensity change, each maximum in Fig. 9(a) is found at the same energy independently of the incident angle and azimuthal orientation of the crystal (cf. Fig. 7). Such a behavior suggests that the maxima arise primarily from an electron scattering property that is averaged over various directions of electron propagation within the crystal (i.e., various free-electron states) and, thus depend on the CB DOS. In Fig. 9(b), we display the CB DOS of solid Ar (Ref. 30) for which we fixed the bottom of the lowest conduction band at the measured value<sup>42</sup> of 0.25 eV above the vacuum level. In contrast to what we found for the phonon background excitation functions, which are proportional to the CB DOS, *maxima* in Fig. 9(a) correlates respectively with *minima* in the CB DOS.

## IV. DISCUSSION

### A. Multiple scattering model

Electron propagation in condensed matter occurs via multiple elastic and inelastic scattering within and between atomic or molecular sites. For a small concentration of molecules isolated in an ordered RGS matrix, this scattering process may be separated for convenience into three parts. First,

the coherent multiple elastic scattering within and between matrix sites is implicitly embodied by using Bloch electron waves inside the solid along with the corresponding transmission and reflection probabilities at the boundaries. Next, the Bloch electrons are allowed to interact with the molecules (i.e., impurities), defects, and phonons, as distinct collision events, by introducing suitable scattering probabilities. Finally, the subsequent multiple incoherent scattering unfolding from the latter individual events is treated as a classical transport phenomena.

### 1. Coherent multiple elastic scattering

First, let us consider the effect of coherent elastic scattering in an ordered solid film. For a pure RGS film the LEED approach is appropriate and it reduces to the matching of the electron wave function outside the crystal to that of the same energy inside.<sup>43</sup> Outside and sufficiently far away from the crystal, we have the incident plane wave, the specular elastic reflection (i.e., 00 beam), and the diffracted beams (i.e., reflected Bragg beams) arising from the periodicity of the surface. Inside the crystal the electron, which experiences multiple elastic scattering, can be either in a surface or an extended Bloch state (i.e., transmitted 00 and Bragg beams) whose energy  $E_{\mathbf{k}}$  as a function of its wave vector  $\mathbf{k}$  defines an energy-band structure. The bottom of the lowest conduction band at  $\mathbf{k}=0$  may be found either above or below the vacuum level and corresponds to the electron affinity of the solid  $V_A$ . As an immediate effect, the energy threshold for an excitation function within a solid is accordingly located at higher or lower energy than in the gas phase. While the intensity of a diffracted beam requires a full knowledge of the multiple scattering inside the solid, its directions is merely given from the conservation, within a reciprocal surface lattice vector  $\mathbf{g}$ , of the electron momentum parallel to the surface.

As a consequence of coherent elastic scattering within the crystal, we have the probability  $P_{\text{en}}$  that an incident electron enters into the solid as a Bloch electron and conversely the probability  $P_{\text{ex}}$  that a Bloch electron leaves the solid along an exit direction (i.e., direction of observation). The probability  $P_{\text{en}}$  is defined from the sum of the intensity of the transmitted Bloch waves in the solid. This quantity also corresponds to the complement of the sum of the specular elastic reflection or the 00 beam and the reflected Bragg beam intensities (i.e., total elastic reflection). Likewise, the probability  $P_{\text{ex}}$  is defined from the sum of the intensity of the transmitted Bloch waves corresponding to the electron being ‘‘incident’’ along the exit direction (i.e., going backward), upon using time-reversal symmetry.<sup>40</sup> The probability  $P_{\text{en}}(P_{\text{ex}})$  thus depends on the entrance (exit) angle as well as the electron energy. Their variation upon the azimuthal orientation of the crystal is also stronger when the incident angle is far away from the normal to the surface. In the case of a fcc (111) crystal,  $P_{\text{en}}(P_{\text{ex}})$  should exhibit in general a threefold symmetry axis, the same as the total elastic reflection. However, if at low energy the specular elastic reflection turns out to be the only beam present (or significantly larger than the Bragg beam intensities), it should results a (quasi) sixfold symmetry axis for both  $P_{\text{en}}$  and  $P_{\text{ex}}$ . Hence, for incoherent collision processes having a *cylindrical symmetry*, the resulting backscattered intensity measured as a function

of the incident energy should exhibit practically the same profile after a  $\phi_0=60^\circ$  azimuthal rotation of the crystal and a mirror symmetry about  $\phi_0=30^\circ$ . As one can see in Fig. 7, these findings realize quite well for the vibrational and phonon excitation functions, considering that our measurement could not be performed under exactly the same experimental conditions as mentioned previously.

### 2. Bloch electron scattering on impurities, phonons, and defects

For an electron propagating in a conduction band of a RGS (i.e., Bloch electron) with an energy below the electronic excitation threshold, scattering events occur primarily on phonons and defects. Owing to the small amount of energy transferred during each collision, this may also be termed quasielastic scattering. In the presence of  $\text{O}_2$  impurities there is, in addition to scattering on more defects, a probability to excite the vibrational and electronic states of the guest molecules. In formal terms, all these processes are described by introducing the scattering probability per unit length (SPUL)  $Q(E_{\mathbf{k}'}, \mathbf{k}', E_{\mathbf{k}}, \mathbf{k})$  that a Bloch electron initially in a state  $|\chi_{\mathbf{k}'}\rangle$  of energy  $E_{\mathbf{k}'}$  is scattered into a final state  $|\chi_{\mathbf{k}}\rangle$  of energy  $E_{\mathbf{k}}$ . Here, to simplify the notation,  $\mathbf{k}'$  and  $\mathbf{k}$  stand for both the electron wave vector and the band index. We note also that the present prototype for the SPUL is more suited for a wave vector  $\mathbf{k}(\mathbf{k}')$  expressed in terms of its direction along with its length corresponding to the scalar energy variable  $E_{\mathbf{k}}(E_{\mathbf{k}'})$ . Following the golden rule,<sup>44</sup> the SPUL is given by

$$Q(E_{\mathbf{k}'}, \mathbf{k}', E_{\mathbf{k}}, \mathbf{k}) = [v_g(\mathbf{k}') \tau(E_{\mathbf{k}'}, \mathbf{k}', E_{\mathbf{k}}, \mathbf{k})]^{-1}, \quad (5a)$$

with

$$\begin{aligned} \tau^{-1}(E_{\mathbf{k}'}, \mathbf{k}', E_{\mathbf{k}}, \mathbf{k}) \\ = (2\pi/\hbar) \sum_{i,f} p_i |\langle \chi_{\mathbf{k}}, f | T | i, \chi_{\mathbf{k}'} \rangle|^2 \delta(E_{\mathbf{k}'} + \varepsilon_i - E_{\mathbf{k}} - \varepsilon_f). \end{aligned} \quad (5b)$$

In Eq. (5a),  $\tau(E_{\mathbf{k}'}, \mathbf{k}', E_{\mathbf{k}}, \mathbf{k})$  is a relaxation time (i.e., the time between scattering events), which depends upon the  $\mathbf{k}'$  and  $\mathbf{k}$  directions, and  $v_g(\mathbf{k}) \equiv \hbar^{-1} |\nabla_{\mathbf{k}} E_{\mathbf{k}}|$  the electron group velocity. The double summations in Eq. (5b) with the thermodynamic probability  $p_i$  of finding the target in the initial states  $|i\rangle$  of energy  $\varepsilon_i$  are included here because both  $|i\rangle$  and the final states  $|f\rangle$  of energy  $\varepsilon_f$  (e.g., phonon and vibrational states) are not probed as such during an electron scattering experiment. At very low temperature, since the solid is mostly in its ground state, one may consider that a Bloch electron suffers scattering only toward lower energy states. Finally,  $T$  is the transition operator that includes all electron scattering mechanisms in the bulk of the solid. Within the Born approximation  $T$  reduces to  $V$ , which, in the pure crystal, is simply given by the electron-defect potential and electron-phonon interaction. However, this approximation is not valid for electron resonant scattering on  $\text{O}_2$  (i.e., the formation of transient negative ions). When an electron attaches on a molecule, hence occupying an empty molecular orbital that may be bonding or antibonding, and then autodetaches; the induced vibrational and electronic excitations may increase by orders of magnitude. Instead in this case,  $T$  might

be separated into a resonant and background (i.e., nonresonant) components, upon applying the projection operator formalism.<sup>45</sup>

### 3. Incoherent multiple elastic and inelastic scattering

The various incoherent multiple elastic and inelastic scatterings suffered by a Bloch electron in the bulk of a solid, following its entrance and prior to its exit at the film-vacuum interface, can be described by using the time-independent Boltzmann transport equation in absence of external fields. A basic phenomenological approach to this transport problem, when the detail of the angular distribution of the backscattered electron intensity is not needed, is to solve the transport equation for plane-parallel systems in the ‘‘two-stream’’ approximation.<sup>46,47</sup> In this approximation we consider instead of  $Q(E_{\mathbf{k}'}, \mathbf{k}', E_{\mathbf{k}}, \mathbf{k})$ , the simpler quantity,  $Q_i(E - E')$ , which represents the angularly integrated SPUL for an electron to lose or gain an energy  $E' - E$ , with  $E'$  and  $E$  its energy before and after the collision. The possible angular anisotropy of a scattering event is simply accounted for by splitting  $Q_i(E - E')$  into two components by introducing of a coefficient of angular anisotropy  $\gamma(E - E')$ .<sup>47</sup> Thus, we have an anisotropic part  $Q_f(E - E') \equiv \gamma(E - E')Q_i(E - E')$ , where scattering only in the forward direction is defined, and an isotropic part  $2Q_r(E - E') \equiv [1 - \gamma(E - E')]Q_i(E - E')$ , where backward scattering is equal to the forward one. As a physical interpretation, the isotropic part

$Q_r(E - E')$  results from all short-range interactions, which include electron resonance processes, whereas the anisotropic part  $Q_f(E - E')$  is more akin to long-range interactions such as dipole scattering. Assuming that the SPUL values are not changing significantly about an initial energy  $E'$ , as it is usually the case for  $E'$  lying within a small energy-loss range  $E - E'$ , we showed previously<sup>46</sup> that by applying the Fourier transform with

$$Q_{r,f}(E - E') = (1/2\pi) \int_{-\infty}^{\infty} ds Q_{r,f}(s) \exp[-s(E - E')], \quad (6)$$

to the transport equation, along with appropriate boundary conditions, yields the following expression:

$$J(E) = (1/2\pi) \int_{-\infty}^{\infty} ds I_0(s) R(s) \exp(-isE), \quad (7)$$

for the backscattered intensity as a function of the final energy  $E$ . In this expression,  $I_0(s)$  is the Fourier transform of the incident current energy distribution entering into the film. It is generally taken to be a unit-normalized Gaussian distribution centered at  $E_0$  of FWHM equal to the instrumental resolution. The term  $R(s)$ , which is the key quantity here, is the Fourier transform of the reflected current energy distribution from a film of thickness  $L$  and is given explicitly by<sup>46</sup>

$$R(s) = \frac{R_{\infty}(M - 1/R_{\infty}) - (1/R_{\infty})(M - R_{\infty}) \exp[-2\varepsilon\beta(s)L(1 - R_{\infty}/1 + R_{\infty})]}{(M - 1/R_{\infty}) - (M - R_{\infty}) \exp[-2\varepsilon\beta(s)L(1 - R_{\infty}/1 + R_{\infty})]}, \quad (8a)$$

where

$$R_{\infty} \equiv R_{\infty}(s) = \frac{1 - [1 - 2Q_r(s)/\beta(s)]^{1/2}}{1 + [1 - 2Q_r(s)/\beta(s)]^{1/2}}. \quad (8b)$$

The latter expression describes the Fourier transform of the reflected current energy distribution, but in the limit of a semi-infinite film<sup>46</sup> [i.e.,  $L \rightarrow \infty$ ]. The quantity  $\beta(s)$  is defined from  $\beta(s) \equiv \alpha - Q_f(s)$  where  $\alpha$  is the total SPUL given by

$$\alpha \equiv \alpha(E') = \int_{-\infty}^{\infty} dE Q_i(E - E'). \quad (9)$$

The latter, which is also considered constant within a small energy-loss range [i.e.,  $\alpha(E) = \alpha(E')$ ], corresponds to the inverse of the total mean free path (MFP) (i.e.,  $\alpha \equiv \lambda^{-1}$ ). The term  $M$  is the reflection coefficient of the underlying substrate and may include elastic as well as inelastic processes. Finally,  $\varepsilon$  is a phenomenological parameter that arises from considering an angular average in a stream direction.<sup>46</sup>

At large film thicknesses (i.e.,  $L \gg \lambda$ ), as one can see in Eq. (8b), the electron reflectivity turns out to be independent of the film thickness, the parameter  $\varepsilon$ , and the nature of the substrate. Since experimentally an HREEL spectrum is no longer changing with increasing coverage, this limit is alter-

natively referred to as a thickness saturation regime. What is more important and not obvious *a priori* in looking at Eq. (8b) is that each SPUL component happens to be normalized to the total SPUL  $\alpha$ . In other words, in this regime, the intensity change of an energy-loss feature is not only the result of a variation in the corresponding SPUL value, but may also be due to a variation in the total SPUL  $\alpha$ .

At intermediate film thicknesses (i.e.,  $L \sim \lambda$ ), Eq. (8) predicts the presence of both thickness saturated along with nonsaturated energy-loss features in the electron reflectivity. This phenomenon, which results essentially from the number of scattering events involved in an energy-loss process, can be qualitatively understood with the help of Fig. 10. Suppose a film of thickness  $L$  within which the incident electrons of energy  $E_0$  [i.e.,  $I(E_0)$ ] cascade down to a final energy  $E$  with an average energy loss per collision of  $\delta E$ , such that  $E_0 \gg E_0 - E \gg \delta E$ . For those electrons that enter, scatter, and then leave the film, thus generating a backscattered intensity  $J(E)$ , one can define the *maximum probed depth*,

$$L_p(E_0, E) \equiv \frac{1}{2} \lambda(E_0)(E_0 - E) / \delta E,$$

where  $\lambda(E_0)$  is the electron MFP, which is considered constant only within a small energy-loss range  $E_0 - E$  about  $E_0$  [i.e.,  $\lambda(E_0) = \lambda(E)$ ]. For a given  $\lambda(E_0)$ ,  $L_p(E_0, E)$  can vary

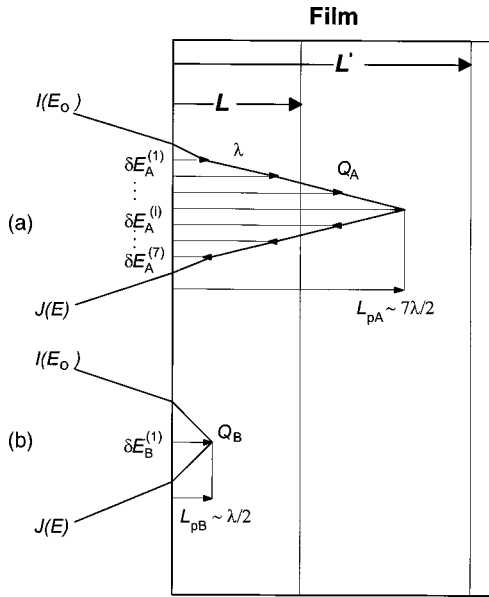


FIG. 10. For those electrons of energy  $E_0$  that enter into the film and cascade down with an average energy loss per collision of  $\delta E$  to a final energy  $E$  and then leave the film, one can define a *maximum probed depth* for the backscattered intensity  $J(E)$ , given by  $L_p(E_0, E) \equiv 1/2\lambda(E_0)(E_0 - E)/\delta E$ , where  $\lambda(E_0)$  is the electron mean-free path considered constant within a small energy-loss range  $E_0 - E$  about  $E_0$ . The consequence of a varying  $L_p(E_0, E)$  on the backscattered intensity  $J(E)$  for a film of thickness  $L$  is different whether the *A* or *B* limit is effective along with the corresponding SPUL event  $Q_A$  or  $Q_B$ .

greatly with the magnitude of  $\delta E$  involved in the multiple-scattering sequence leading to an energy-loss feature at  $\Delta E = E_0 - E$ . For instance,  $L_p(E_0, E)$  is decreasing by more than one order of magnitude with the leading energy-loss event changing from a phonon excitation at  $\delta E \sim 0.01$  eV (case *A* in Fig. 10) to the  $\nu = 1$  vibrational excitation at  $\delta E \sim 0.2$  eV (case *B* in Fig. 10). Besides,  $L_p(E_0, E)$  is directly proportional to  $\lambda(E_0)$ . The consequence of a varying  $L_p(E_0, E)$  on the backscattered intensity  $J(E)$  for a film of thickness  $L$  is different whether the *A* or *B* limit is effective along with the corresponding SPUL event  $Q_A$  or  $Q_B$ , as illustrated in Fig. 10. In the *A* limit, where  $E_0 - E = n\delta E_A$  with  $n \gg 1$  and  $L_{pA}(E_0, E) > L$ , the backscattered intensity varies according to  $J(E) \sim (L/L_{pA})I(E_0)Q_A^n L$  and therefore in effect as  $J(E) \propto Q_A^n/\lambda(E_0) = Q_A^n \alpha(E_0)$ . This may reflect approximately the CB DOS as shown previously for multiple phonon losses in RGS. In the *B* limit, where  $E_0 - E = \delta E_B$  and  $L_{pB}(E_0, E) < L$ , the backscattered intensity is thickness saturated with  $J(E) \sim I(E_0)Q_B L_{pB}$  and thus behaves as  $J(E) \propto Q_B \lambda(E_0) = Q_B/\alpha(E_0)$ . Since in this case  $J(E)$  depends on the ratio of a SPUL value to the total SPUL  $\alpha(E_0)$ , the intensity of an energy-loss maximum may be modulated by a factor that is roughly inversely proportional to the CB DOS.

At small film thicknesses (i.e.,  $L \ll \lambda$ ), let us consider the inelastic reflectivity arising from various single inelastic events but along with coherent multiple elastic scattering, which is already embodied in the Bloch electron waves. Considering further that the elastic reflectivity of the sub-

strate  $M_e$  is much larger than that of the semi-infinite film  $R_{\infty e}$ , Eq. (8a) can be reduced to

$$R_{L \rightarrow 0}(s) \cong M_e + \varepsilon Q_{ri}(s)L + M_e 2\varepsilon Q_{ri}(s)L + M_e 2\varepsilon Q_{fi}(s)L. \quad (10)$$

In this expression, the second term on the right-hand side is the inelastic contribution originating directly from the film. Only the isotropic SPUL component,  $Q_{ri}(s)$ , is present here owing to the backscattering geometry. The following two terms account for the inelastic contributions that are mediated by the elastic reflection from the substrate. Both isotropic and anisotropic SPUL components,  $Q_{ri}(s)$  and  $Q_{fi}(s)$ , multiplied by the substrate reflectivity  $M_e$  are contributing. The factor two merely accounts for the electron path being twice that of the direct contribution. Therefore, the inelastic reflectivity, though it depends somewhat upon the nature of the substrate, is on the whole directly proportional to the SPUL values as well as the thickness of the film.

Attributing the relative intensity change of the intrinsic features for different scattering angles to the entrance  $P_{en}$  and exit  $P_{ex}$  probabilities and looking at Eqs. (8) and (10), the correlation between the intrinsic features and the inverse of the CB DOS may be twofold in principle. First, such a correlation may be traced back to variations in the individual vibrational SPUL,  $Q_i(E - E')$ . Under electron resonance condition, the vibrational excitation is dependent on the resonance lifetime, which in turn varies with the inverse of the CB DOS of the host medium, as described by Eq. (4). Second, as suggested qualitatively by the concept of the maximum probed depth in the case *B*, it may as well be due to variations in the electron transport property, which under the thickness saturation regime depends upon the MFP or the inverse of the total SPUL  $\alpha(E_0)$ .

### B. Variation of the resonant scattering probability

The presence of features akin to the CB DOS in a resonant vibrational excitation function is expected from the semiclassical model with the transfer of energy to the nuclei given by Eq. (4). As such, this formula illustrates that a significant energy absorbed by the nuclei and thus the presence of a vibrational progression in a HREEL spectrum is not necessarily the result of a long-lived transient anion state, as it is often thought to be the case, but may also occur in the case of a relatively short-lived anion state provided that a sufficiently large vibrational coupling strength [i.e.,  $F_r(R) = dV_r(R)/dR$ ] exists. Taking the slope of  ${}^4\Sigma_u^-$  anion potential energy curve at a resonance energy of 9 eV along with the energy width  $\Gamma$  of 3.4 eV, as obtained by Noble and Burke<sup>13</sup> from *R*-matrix method, we calculate that an energy as large as 0.1 eV can be imparted to the nuclei.<sup>31</sup> Since in effect the energy of the resonance depends upon the internuclear distance, i.e.,  $E_r(R) = V_r(R) - V_G(R)$ , the same applies over the resonance energy range of about 10 eV owing essentially to the overlap of the nuclear wave function of the transient anion with that of the ground state (i.e., Franck-Condon factor). Alternatively, this energy range can be seen as the result of resonant scattering events taking random snapshots of a molecule whose resonance energy fluctuates due to the nuclear motion about the equilibrium position in the ground state. In absence of potential energy curve cross-

ings within the Franck-Condon region, the factor  $F_r(R)$  in Eq. (4) varies slowly as a function of the internuclear distance  $R$ . More importantly, as the transient anion potential energy curve  $V_r(R)$  is, in a first approximation, only slightly and rigidly shifted down by the polarization of the surrounding medium,  $F_r(R)$ , which is derived from it, is virtually the same in both gas and condensed phase. On the contrary, the lifetime of the resonance  $\tau[E_r(R)]$ , whose inverse is explicitly given by

$$\tau^{-1}[E_r(R)] \cong (2\pi/\hbar) |V_{d,E_r}|^2 D[E_r(R)],$$

[cf. Eq. (2)] is directly linked to the CB DOS of the host medium, i.e.,  $D[E_r(R)]$ . The remaining factor, which contains the matrix element responsible for the decay  $V_{d,E_r}$ , is akin to a tunneling effect. More specifically for a spherically symmetric target, it arises from the electron penetration through the centrifugal barrier and yields essentially a monotonous behavior in energy.<sup>48</sup> Owing to its relatively short-range character, it is also not expected to change significantly on going from the gas to the condensed phase. Consequently, the amount of energy transferred to the nuclei [c.f., Eq. (4)] and thus the *excitation of overtones* along with their vibrational scattering probabilities vary, via the modification of the resonance lifetime, according to the *opposite* of the CB DOS of the host medium. It should be further noticed, that higher is an overtone, the more sensitive it is to a change in the resonance lifetime. This is verified experimentally in Fig. 4 from comparing, for instance, the extent of the vibrational progression in the HREEL spectrum at  $E_0=7.9$  eV with that at 7.2 eV or the one observed at  $E_0=5$  eV with that at 4 eV. More generally, the strongest variation should be found in the case of molecules embedded in ordered solids or crystals provided that, before and after the formation of a transient anion state, the electron propagates within a well-defined energy-band structure.

### C. Variation of the electron transport property

The effect of the variation in the electron transport property, which is qualitatively explained with the idea of the *maximum probed depth* in the  $A$  and  $B$  limit, can be more exactly illustrated by calculating the backscattered intensity  $J(E)$  from a 20-layer film of 1%  $O_2$  in Ar with the two-stream approximation. In relation to the case  $A$ , let  $Q_{t,A}(E-E')/\alpha(E)$  be a normalized electron SPUL for phonon excitations that follows approximately the phonon frequency distribution in solid Ar, as shown in Fig. 11(a), with a constant coefficient of angular anisotropy  $\gamma_A(E-E')$  of 0.5. The elastic reflectivity of the underlying substrate  $M_e$  is fixed at 0.3 and for simplicity  $\varepsilon$  is taken equal to one. It should be mentioned that these parameters are the same as those used to explain the CB DOS effects in the pure solid film of Ar.<sup>28</sup> In connection to the case  $B$ , let us consider along with these parameters, a small  $O_2$  concentration with a constant isotropic electron SPUL  $Q_{t,B}(E-E')$ . The latter is simply chosen to follow the relative values of the gas-phase electron scattering cross sections for the vibrational  $X^3\Sigma_g^-(v=0,1,2,3,4,5,6)$  and electronic  $a^1\Delta_g(v=0)$  excitations at an impact energy of about 9 eV, as shown in Table I.

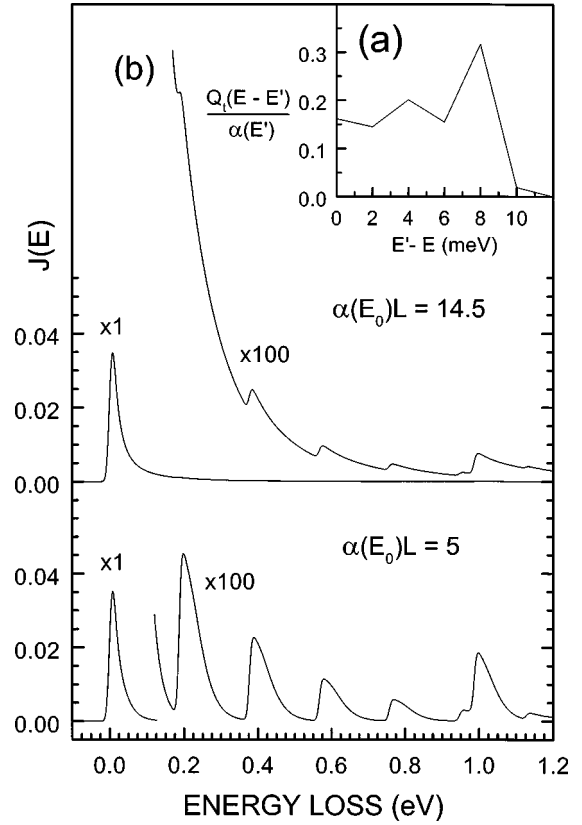


FIG. 11. (a) Normalized electron scattering probability per unit length  $Q_t(E-E')/\alpha(E)$  for elastic scattering and phonon excitations, which follows approximately the phonon frequency distribution in solid Ar, used in the two-stream model to generate in (b) the backscattered energy-loss distribution  $J(E)$  from a 20-layer film of 1%  $O_2$  in Ar for two different values of the dimensionless variable  $\alpha(E_0)L$ .

Using Eqs. (7) and (8) with  $I_0(s)$  the incident current energy distribution centered around  $E_0$  and having a FWHM equal to the instrumental resolution (i.e., 15 meV), we show in Fig. 11(b) the calculated backscattered intensity  $J(E)$  from a 20-layer film as a function of the energy loss  $\Delta E = E_0 - E$  for two different values of the dimensionless parameter  $\alpha(E_0)L$ . With the above choice of parameters, the elastic, phonon background, vibrational progression, and electronic intensities are close to what is observed experimentally for the same film thickness and intensity gain (Fig. 4). The calculated energy-loss tail, which is due to multiple scattering on phonons, increases with  $\alpha(E_0)L$  as in the case of pure solid film of Ar.<sup>28</sup> On the contrary, the superimposed features, which are essentially due to *single* vibrational- or electronic-loss events on  $O_2$  in the matrix, are attenuated on the whole with  $\alpha(E_0)L$ .

Taking the same fixed parameters, we present in Fig. 12 the variation of  $J(E)$  for the elastic peak at  $\Delta E = 0$  eV, the  $v = 1, 2$  vibrational losses along with the phonon background at  $\Delta E = 0.18$  and 0.37 eV as a function of  $\alpha(E_0)L$ . Here, the value of  $\alpha(E_0)$  is practically the total SPUL for phonon excitations since the relatively small and fixed (i.e.,  $\sim 1.3 \times 10^{-2}$  layer<sup>-1</sup>) contribution from the  $O_2$  molecules. The trend in the multiplication factors follows the inverse of the vibrational SPUL values (Table I). The calculated intensity of the elastic peak (solid line) is the same over most of the

TABLE I. Angularly integrated electron scattering probability per unit length  $Q_{i,B}(10^{-3} \text{ layer}^{-1})$  for the excitations of the vibrational  $X^3\Sigma_g^-$  ( $v=0,1,2,3,4,5,6$ ) and electronic  $a^1\Delta_g$  ( $v=0$ ) modes of  $O_2$  isolated in an Ar matrix (1% volume).  $h\nu$  (meV) is the excitation energy of a mode. The  $Q_{i,B}$  values follow approximately the corresponding gas-phase cross sections at an incident electron energy of 9 eV.

	$X^3\Sigma_g^-$						$a^1\Delta_g$ $v=0$	
	$v=0$	$v=1$	$v=2$	$v=3$	$v=4$	$v=5$		$v=6$
$h\nu$	0	190	380	570	760	950	1130	980
$Q_{i,B}$	10	1	0.5	0.25	0.125	0.063	0.04	0.375

$\alpha(E_0)L$  range. This can be understood qualitatively since the elastic SPUL of solid Ar augments proportionally with  $\alpha(E_0)$  while the *maximum probed depth* decreases according to the inverse of  $\alpha(E_0)$  [i.e.,  $\lambda(E_0)$ ], thus making the resulting backscattered intensity unchanged. Each phonon background intensities at  $\Delta E=0.18$  and  $0.37$  eV (dashed lines) increases with  $\alpha(E_0)L$  up to a saturation point beyond which it becomes practically constant. The saturation point in each case corresponds to the value of the maximum probed depth,  $L_{pA} = \frac{1}{2}\lambda(E_0)\Delta E/\delta E$ , being about equal to the present film thickness ( $L=20$  layers). Hence, provided that the film thickness is appropriate, the phonon background intensity can reflect variations in the total SPUL  $\alpha(E_0)$  and therefore,  $D(E_0)$ , as in the pure Ar case.<sup>28</sup> The calculated intensities for  $v=1$  and  $2$  vibrations (solid lines) exhibit a shallow minimum with a rise in magnitude for small value of  $\alpha(E_0)L$ . For large value of  $\alpha(E_0)L$ , both vibrational energy-loss intensities follow the same general trend as their respective phonon background, since each of them turns out to be a relatively small quantity superimposed on the latter. However, the net vibrational energy-loss intensity, resulting from the subtraction of the corresponding phonon background, varies essentially according to the common factor  $1/\alpha(E_0)$ . This is directly apparent in Fig. 12 from the merging of the vibrational curves

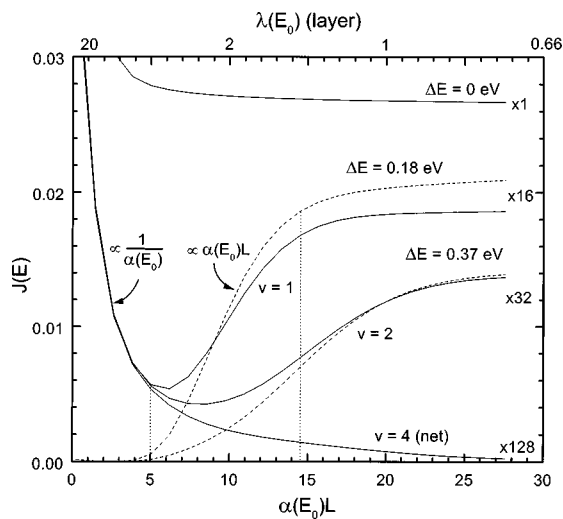


FIG. 12. Backscattered intensity  $J(E)$  for the elastic peak ( $\Delta E = 0$  eV), the  $v=1,2$  vibrational losses along with their corresponding phonon background at the energy losses  $\Delta E=0.18$  and  $0.37$  eV for a 20-layer film of 1%  $O_2$  in Ar as a function of the dimensionless variable  $\alpha(E_0)L$ . The net backscattered intensity  $J(E)$  for the overtone  $v=4$  results from the subtraction of its corresponding phonon background.

at small  $\alpha(E_0)L$  values where the phonon background is negligible. The same factor is found for the net intensity of the higher overtones (e.g.,  $v=4$  in Fig. 12) as well as the electronic energy loss. This common behavior, which we consider to be the key observation here, merely stems from the fact that for  $\alpha(E_0)L \geq 0.5$ , we have  $L_{pB} \leq L = 20$  layers. Under this condition, all *single* energy-loss contributions are already thickness saturated and hence subjected to the SPUL ratio as mentioned previously in connection with Eq. (8).

In Fig. 12, the two vertical-dotted lines, at which the energy-loss calculations in Fig. 11(b) were performed, define the typical range of  $\alpha(E_0)L$  that can explain the phonon background features observed experimentally at 20 layers. Within these boundaries, the calculated intensities for  $\Delta E = 0.18$  and  $0.37$  eV vary from about 10% and 5% (i.e., low limit) up to a maximum of about 90% and 50% (i.e., high limit), respectively, of their saturated value at the right end of the figure. The latter behavior is observed experimentally in Fig. 8, where the intensity of the feature due to the phonon background around 6.8 eV within the  $v=2$  profile reaches at 20 layers about 50% of its value at 50 layer, which is close to the saturation. Between the same two limits, the net intensities of the vibrational and electronic energy losses are calculated to vary altogether by a factor of up to about three. As a result, besides the maximum due to multiple scattering on phonon for large value of  $\alpha(E_0)L$ , a small maximum is expected in the vibrational scattered intensity whenever a minimum occur in the phonon background. The latter maximum is more specifically considered as *intrinsic* since it *belongs solely* to the vibrational intensity whereas the former, being merely *additive*, is classified as *extrinsic*. Given an energy-loss value and a film thickness  $L$ , the relative amplitude between both maxima depends essentially upon the lower and upper value reached by the total SPUL  $\alpha(E_0)$ . For example in Figs. 11(b) and 12, the value of  $J(E)$  for  $v=2$  at the low limit is about the same as that at the high limit, whereas the value of  $J(E)$  for  $v=1$  at the low limit, which is a factor of two larger than in the  $v=2$  case, is relatively much smaller than its high limit value. Assuming that the vibrational and electronic SPUL values are constant, the net intensity changes due to variation of  $\alpha(E_0)$  between the two present limits is found to be the same, regardless whether the inelastic events arise from resonant or nonresonant scattering. On the other hand, the observation of distinct intensity changes among the energy losses, such as selective vibrational excitations, can only be attributed to variations in the corresponding SPUL value. For instance in the HREEL spectrum of Fig. 4, the  $v=3,4,5$  overtones at  $E_0=7.9$  eV, which compare in intensity to the  $a^1\Delta_g$  electronic loss, have almost

disappeared at  $E_0 = 7.2$  eV whereas the electronic loss is only slightly attenuated. The same effect is also observed in going from  $E_0 = 5$  to 4 eV with the electronic intensity being alike.

## V. CONCLUSION

Definitive identification of an electron resonance in the condensed phase must involve analysis beyond the observation of selective vibrational and electronic excitations as well as the presence of a strong variation with the impact energy in the corresponding excitation functions, as in the gas phase. In the condensed phase, multiple elastic, and inelastic electron scattering may yield additional features within an excitation function. The present work dealt more specifically with the changes that occur in the electron-induced vibrational excitation of a matrix-isolated molecule and that are due to variations in the CB DOS of the host medium. As an experimental model, we chose to study  $O_2$  isolated in an ordered Ar matrix.

Growth of an Ar film on the Pt(111) at 16 K is highly ordered up to at least 50 layers and proceeds along the normal to the (111) planes of the fcc single crystal of Ar. The crystal structure and the CB DOS of the Ar-matrix film with 1% volume of  $O_2$  are not much different from that of the pure solid. The scattered electron intensities corresponding to vibrational excitations of the matrix-isolated molecule exhibit a strong incident energy dependence with two different contributions, which can be classified either as extrinsic or intrinsic features. Except for a relative change in intensity, all these features remain essentially at the same energy for different scattering angles. The relative change in intensity is attributed to the angular dependence of the electron entrance  $P_{en}$  and exit  $P_{ex}$  probabilities at the crystal-vacuum interface.

The extrinsic features arise from the energy dependence of the superimposed multiple-scattering phonon background that reflects the CB DOS of the host medium. The intrinsic features, which differ from the extrinsic ones as they grow and saturate more quickly with the thickness of the film, correspond to a modulation of the vibrational scattered intensities as a function of the incident energy. The origin of this modulation is further shown to be twofold. It can result from the variation in the individual vibrational SPUL owing to changes of the resonance lifetime, which follows the inverse of the CB DOS of the surrounding medium. The higher overtone or combination vibrations, which correspond to large energy transfers to the nuclei, are the most sensitive modes to a change in the resonance lifetime. Modulation of the vibrational and electronic loss intensities can also be caused by the variation in the electron transport property or MFP, which under a thickness saturation regime may follow the inverse of the CB DOS. However, as shown by multiple scattering model calculations, such a variation can only account for a common and limited modulation.

As a final remark, one may expect in the presence of strong coupling to phonons that variations in the CB DOS should be reflected in the energy dependence of the multiphonon-loss signal similar to the case of vibrational excitation. With increasing anion lifetime, a larger lattice distortion results and thus an increase of energy loss to multiphonon excitations of the crystal after the decay of the resonance.

## ACKNOWLEDGMENTS

This research was sponsored by the Medical Research Council of Canada. We would like to thank D. Robillard for his technical assistance.

- 
- <sup>1</sup>G. J. Schulz, *Rev. Mod. Phys.* **45**, 423 (1973).  
<sup>2</sup>R. I. Hall and F. H. Read, in *Electron-Molecule Collisions*, edited by H. B. Gilbody, W. R. Newell, F. H. Read, and A. C. H. Smith (Plenum, New York, 1984), p. 378.  
<sup>3</sup>M. Allan, *J. Electron Spectrosc. Relat. Phenom.* **48**, 219 (1989).  
<sup>4</sup>L. Sanche, in *Excess Electrons in Dielectric Media*, edited by C. Ferradini and J. P. Jay-Gerin (CRC, Boca Raton, 1991), p. 1; L. Sanche, *J. Phys. B* **23**, 1597 (1990).  
<sup>5</sup>R. E. Palmer and P. J. Rous, *Rev. Mod. Phys.* **64**, 383 (1992); R. E. Palmer, *Prog. Surf. Sci.* **41**, 51 (1992).  
<sup>6</sup>K. Jacobi and M. Bertolo, *Phys. Rev. B* **42**, 3733 (1990); M. Gruyters and K. Jacobi, *Chem. Phys. Lett.* **225**, 309 (1994).  
<sup>7</sup>D. Schmeisser, J. E. Demuth, and Ph. Avouris, *Phys. Rev. B* **26**, 4857 (1982).  
<sup>8</sup>M. Allan, *J. Phys. B* **28**, 4329 (1995).  
<sup>9</sup>M. Allan, *J. Phys. B* **28**, 5163 (1995).  
<sup>10</sup>A. G. Middleton, P. J. O. Teubner, and M. J. Brunger, *Phys. Rev. Lett.* **69**, 2495 (1992); A. G. Middleton, M. J. Brunger, P. J. O. Teubner, M. W. B. Anderson, C. J. Noble, G. Wöste, K. Blum, P. G. Burke, and C. Fullerton, *J. Phys. B* **27**, 4057 (1994).  
<sup>11</sup>J. P. Ziesel, J. Randell, D. Field, S. L. Lunt, G. Mrotzek, and P. Martin, *J. Phys. B* **26**, 527 (1993).  
<sup>12</sup>T. W. Shin and C. J. Sweeney, *Phys. Rev. A* **47**, 1006 (1993); **48**, 1214 (1993).  
<sup>13</sup>K. Higgins, P. G. Burke, and C. J. Noble, *J. Phys. B* **27**, 3203 (1994); K. Higgins, C. J. Gillan, C. J. Noble, and P. G. Burke, *ibid.* **28**, 3391 (1995).  
<sup>14</sup>C. J. Noble and P. G. Burke, *Phys. Rev. Lett.* **68**, 2011 (1992).  
<sup>15</sup>D. Teillet-Billy, L. Malegat, and J. P. Gauyacq, *J. Phys. B* **20**, 3201 (1987).  
<sup>16</sup>G. Das, A. C. Wahl, W. T. Zemke, and W. C. Stwalley, *J. Chem. Phys.* **68**, 4252 (1978); G. Das, W. T. Zemke, and W. C. Stwalley, *ibid.* **72**, 2327 (1979); H. H. Michels, *Adv. Chem. Phys.* **45**, 225 (1981).  
<sup>17</sup>L. Sanche and M. Michaud, *Phys. Rev. Lett.* **47**, 1008 (1981).  
<sup>18</sup>S. F. Wong, M. J. Boness, and G. J. Schulz, *Phys. Rev. Lett.* **31**, 969 (1973).  
<sup>19</sup>E. Feshbach, *Ann. Phys. (N.Y.)* **5**, 357 (1958); U. Fano, *Phys. Rev.* **124**, 1866 (1961); P. W. Anderson, *ibid.* **124**, 41 (1961).  
<sup>20</sup>A. Messiah, *Quantum Mechanics* (Wiley, New York, 1961), Vol. I, p. 401.  
<sup>21</sup>T. F. O'Malley, *Phys. Rev.* **137**, A1668 (1965); J. C. Y. Chen, *Phys. Rev.* **148**, 66 (1966).  
<sup>22</sup>W. Domcke, *Phys. Rep.* **208**, 97 (1991); *J. Phys. B* **14**, 4889 (1981); W. Domcke and L. S. Cederbaum, *Phys. Rev. A* **16**, 1465 (1977).  
<sup>23</sup>D. L. Mills, *Phys. Rev. B* **45**, 13 221 (1992).  
<sup>24</sup>N. W. Ashcroft and D. W. Mermin, *Solid Phase Physics* (Holt,

- Rinehart and Winston, New York, 1976), Chap. 8.
- <sup>25</sup>U. Rössler, in *Rare-Gas Solids*, edited by M. L. Klein and J. A. Venables (Academic, New York, 1975), p. 505.
- <sup>26</sup>B. Sonntag, in *Rare-Gas Solids* (Ref. 25), p. 1021.
- <sup>27</sup>N. Schwentner, E.-E. Koch, and J. Jortner, *Condensed Rare Gases* (Springer-Verlag, Berlin, 1985), p. 22.
- <sup>28</sup>M. Michaud, L. Sanche, T. Goulet, and J.-P. Jay-Gerin, *Phys. Rev. Lett.* **66**, 1930 (1991); M. Michaud, P. Cloutier, and L. Sanche, *Phys. Rev. B* **44**, 10 485 (1991).
- <sup>29</sup>T. Goulet, J.-M. Jung, M. Michaud, J.-P. Jay-Gerin, and L. Sanche, *Phys. Rev. B* **50**, 5101 (1994).
- <sup>30</sup>N. C. Bacalis, D. A. Papaconstantopoulos, and W. E. Pickett, *Phys. Rev. B* **38**, 6218 (1988).
- <sup>31</sup>M. Michaud, M. Lepage, and L. Sanche, *Phys. Rev. Lett.* **81**, 2807 (1998).
- <sup>32</sup>L. Sanche and M. Michaud, *Phys. Rev. B* **30**, 6078 (1984).
- <sup>33</sup>M. Michaud, P. Cloutier, and L. Sanche, *Rev. Sci. Instrum.* **66**, 2661 (1995).
- <sup>34</sup>H. Kuhlenbeck, M. Lepage, M. Michaud, L. Sanche, H. Sambe, and D. E. Ramaker, *Chem. Phys. Lett.* **238**, 93 (1995).
- <sup>35</sup>C. Gaubert, R. Baudoing, Y. Gauthier, M. Michaud, and L. Sanche, *Appl. Surf. Sci.* **25**, 195 (1986).
- <sup>36</sup>G. Bader, G. Perluzzo, L. G. Caron, and L. Sanche, *Phys. Rev. B* **26**, 6019 (1982).
- <sup>37</sup>M. Michaud, L. Sanche, C. Gaubert, and R. Baudoing, *Surf. Sci.* **205**, 447 (1988).
- <sup>38</sup>A. J. Cruz and G. E. Lopez, *J. Chem. Phys.* **104**, 4294 (1996); in *Chemistry and Physics of Matrix-Isolation Species*, edited by L. Andrews and M. Moskovits (North-Holland, Amsterdam, 1989); in *Matrix Isolation Spectroscopy*, edited by A. J. Barnes, W. J. Orville-Thomas, A. Muller, and R. Gaufres (Reidel, Holland, 1981); in *Vibrational Spectroscopy of Trapped Species*, edited by H. E. Hallan (Wiley, London, 1973).
- <sup>39</sup>R. Azria, L. Parenteau, and L. Sanche, *Phys. Rev. Lett.* **59**, 638 (1987).
- <sup>40</sup>D. P. Woodruff, and B. W. Holland, *Phys. Lett.* **31A**, 207 (1970).
- <sup>41</sup>M. Michaud, P. Cloutier, and L. Sanche, *Phys. Rev. B* **49**, 8360 (1994).
- <sup>42</sup>N. Schwentner, E.-E. Koch, and J. Jortner, *Electronic Excitations in Condensed Rare Gases* (Springer-Verlag, Berlin, 1985), p. 22; G. Perluzzo, G. Bader, L. G. Caron, and L. Sanche, *Phys. Rev. Lett.* **55**, 545 (1985).
- <sup>43</sup>J. B. Pendry, *Low-Energy Electron Diffraction* (Academic, New York, 1971); S. Y. Tong, in *Progress in Surface Science*, edited by S. G. Davison (Pergamon, London, 1975), Vol. 7, p. 1; L. J. Clarke, *Surface Crystallography: An Introduction to Low-Energy Electron Diffraction* (Wiley, New York, 1985).
- <sup>44</sup>G. Baym, *Lectures on Quantum Mechanics* (Benjamin, Reading, MA, 1974), p. 251.
- <sup>45</sup>W. Domcke, *Phys. Rev. A* **28**, 2777 (1983).
- <sup>46</sup>M. Michaud and L. Sanche, *Phys. Rev. B* **30**, 6067 (1984).
- <sup>47</sup>M. Michaud and L. Sanche, *Phys. Rev. A* **36**, 4672 (1987); **36**, 4684 (1987).
- <sup>48</sup>A. R. P. Rau, in *Electronic and Atomic Collisions*, edited by J. Eichler, I. V. Hertel, and N. Stolterfoht (Elsevier, New York, 1984), p. 711.